

# *Comparison of terrain following and cut cell grids using a non-hydrostatic model*

Article

Accepted Version

Shaw, J. and Weller, H. ORCID: <https://orcid.org/0000-0003-4553-7082> (2016) Comparison of terrain following and cut cell grids using a non-hydrostatic model. *Monthly Weather Review*, 144 (6). pp. 2085-2099. ISSN 0027-0644 doi: 10.1175/MWR-D-15-0226.1 Available at <https://centaur.reading.ac.uk/57625/>

It is advisable to refer to the publisher's version if you intend to cite from the work. See [Guidance on citing](#).

To link to this article DOI: <http://dx.doi.org/10.1175/MWR-D-15-0226.1>

Publisher: American Meteorological Society

All outputs in CentAUR are protected by Intellectual Property Rights law, including copyright law. Copyright and IPR is retained by the creators or other copyright holders. Terms and conditions for use of this material are defined in the [End User Agreement](#).

[www.reading.ac.uk/centaur](http://www.reading.ac.uk/centaur)

**CentAUR**

Central Archive at the University of Reading



1

# Comparison of Terrain Following and Cut Cell Grids using a

2

## Non-Hydrostatic Model

3 James Shaw\* and Hilary Weller

4 *Department of Meteorology, University of Reading, Reading, United Kingdom*

5 \*Corresponding author address: Department of Meteorology, University of Reading, Earley Gate,  
6 PO Box 243, Reading, RG6 6BB, UK.  
7 E-mail: js102@zepler.net

## ABSTRACT

8 Terrain following coordinates are widely used in operational models but the  
9 cut cell method has been proposed as an alternative that can more accurately  
10 represent atmospheric dynamics over steep orography. Because the type of  
11 grid is usually chosen during model implementation, it becomes necessary to  
12 use different models to compare the accuracy of different grids. In contrast,  
13 here a C-grid finite volume model enables a like-for-like comparison of terrain  
14 following and cut cell grids. A series of standard two-dimensional tests using  
15 idealised terrain are performed: tracer advection in a prescribed horizontal ve-  
16 locity field, a test starting from resting initial conditions, and orographically  
17 induced gravity waves described by nonhydrostatic dynamics. In addition,  
18 three new tests are formulated: a more challenging resting atmosphere case,  
19 and two new advection tests having a velocity field that is everywhere tan-  
20 gential to the terrain following coordinate surfaces. These new tests present a  
21 challenge on cut cell grids. The results of the advection tests demonstrate that  
22 accuracy depends primarily upon alignment of the flow with the grid rather  
23 than grid orthogonality. A resting atmosphere is well-maintained on all grids.  
24 In the gravity waves test, results on all grids are in good agreement with exist-  
25 ing results from the literature, although terrain following velocity fields lead  
26 to errors on cut cell grids. Due to semi-implicit timestepping and an upwind-  
27 biased, explicit advection scheme, there are no timestep restrictions associated  
28 with small cut cells. We do not find the significant advantages of cut cells or  
29 smoothed coordinates that other authors find.

30 **1. Introduction**

31 Representing orography accurately in numerical weather prediction systems is necessary to  
32 model downslope winds and local precipitation. Orography also exerts strong non-local influ-  
33 ences: from the latent heat release due to convection, by directly forcing gravity waves and plan-  
34 etary waves, and by the atmospheric response to form drag and gravity wave drag. There are two  
35 main approaches to representing orography on a grid: terrain following layers and cut cells, with  
36 the immersed (or embedded) boundary method (Simon et al. 2012) being similar to a cut cell ap-  
37 proach. All methods align cells in vertical columns. Most models are designed for a particular  
38 type of grid, and the study by Good et al. (2014) compared cut cell results with terrain following  
39 solutions implemented within different models. Instead, this study uses a single model to enable a  
40 like-for-like comparison between solutions using terrain following and cut cell grids.

41 With increasing horizontal model resolution, the discrete representation of terrain can become  
42 steeper, making accurate calculation of the horizontal pressure gradient more difficult when using  
43 terrain following layers (Gary 1973; Steppeler et al. 2002). Numerical errors in this calculation  
44 result in spurious winds and can cause numerical instability (Fast 2003; Webster et al. 2003). Cut  
45 cell methods seek to reduce the error that is associated with steep orography.

46 With terrain following (TF) layers the terrain's influence decays with height so that the bot-  
47 tommost layers follow the underlying surface closely while the uppermost layers are flat. There  
48 are two main approaches to minimizing errors associated with TF layers. First, by smoothing  
49 the effects of terrain with height, the influence of the terrain is reduced, hence errors in the cal-  
50 culated horizontal pressure gradient are also reduced aloft (Schär et al. 2002; Leuenberger et al.  
51 2010; Klemp 2011). However, the error is not reduced at the ground where steep terrain remains  
52 unmodified.

53 Second, numerical errors can also be reduced by improving the accuracy in calculating the hor-  
54 izontal pressure gradient itself. TF layers are usually implemented using a coordinate transforma-  
55 tion onto a rectangular computational domain, which introduces metric terms into the equations of  
56 motion. The techniques proposed by Klemp (2011) and Zängl (2012) both involve interpolation  
57 onto  $z$ -levels in order to calculate the horizontal pressure gradient. This gave them the flexibility to  
58 design more accurate horizontal pressure gradient discretizations using more appropriate stencils.  
59 The technique proposed by Weller and Shahrokhi (2014) involved calculating pressure gradients  
60 in the direction aligned with the grid, thus ensuring curl-free pressure gradients and improving  
61 accuracy.

62 Despite their associated numerical errors, TF layers are in widespread operational use (Step-  
63 peler et al. 2003). They are attractive because their rectangular structure is simple to process by  
64 computer and link with parameterisations, and boundary layer resolution can be increased with  
65 variable spacing of vertical layers (Schär et al. 2002).

66 Cut cells is an alternative method in which the grid does not follow the terrain but, instead, cells  
67 that lie entirely below the terrain are removed, and those that intersect the surface are modified in  
68 shape so that they more closely fit the terrain. The resulting grid is orthogonal everywhere except  
69 near cells that have been cut. Hence, errors are still introduced when calculating the horizontal  
70 pressure gradient between cut and uncut cells.

71 The cut cell method can create some very small cells which reduce computational efficiency  
72 (Klein et al. 2009), and several approaches have been tried to alleviate the problem. Yamazaki  
73 and Satomura (2010) combine small cells with horizontally or vertically adjacent cells. Steppeler  
74 et al. (2002) employ a thin-wall appoximation to increase the computational volume of small cells  
75 without altering the terrain. Jebens et al. (2011) avoid the timestep restriction associated with  
76 explicit schemes by using an implicit method for cut cells and a semi-explicit method elsewhere.

77 Some studies have shown examples where cut cells produce more accurate results when com-  
78 pared to TF coordinates. Spurious winds seen in TF coordinates are not present with cut cells and  
79 errors do not increase with steeper terrain (Good et al. 2014). A comparison of TF and cut cells  
80 using real initial data by Steppeler et al. (2013) found that five-day forecasts of precipitation and  
81 wind over Asia in January 1989 were more accurate in the cut cell model, although this result was  
82 dependent on using an old version of a model.

83 Another alternative method is the eta coordinate, described by Mesinger et al. (1988). This  
84 transformation, expressed in pressure coordinates, quantises the surface pressure at each grid box  
85 using prescribed geometric heights. This results in terrain profiles having a staircase pattern which  
86 is known as ‘step’ orography. The eta coordinate improves the accuracy of the horizontal pressure  
87 gradient calculation compared to the sigma coordinate (Mesinger et al. 1988).

88 In an experiment of orographically induced gravity waves, Gallus and Klemp (2000) found that  
89 horizontal flow along the lee slope was artificially weak in the Eta model. Mesinger et al. (2012)  
90 offer an explanation for this behaviour: air flowing along the lee slope cannot travel diagonally  
91 downwards but must first travel horizontally, then vertically downward. However, lee slope winds  
92 are weakened because some of the air continues to be transported horizontally aloft.

93 Mesinger et al. (2012) refined the formulation to allow diagonal transport of momentum and  
94 temperature immediately above sloping terrain. This arrangement is similar to the finite volume  
95 cut cell method. The new method improved test results, increasing lee slope winds by  $4 \text{ m s}^{-1}$  to  
96  $5 \text{ m s}^{-1}$  (Mesinger et al. 2012).

97 This study uses a modified version of the fully-compressible model from Weller and Shahrokhi  
98 (2014) to enable a like-for-like comparison between terrain following and cut cell grids for ide-  
99 alised, two-dimensional test cases from the literature. Section 2 presents the formulation of the  
100 terrain following and cut cell grids used in the experiments that follow. In section 3 we give the

101 governing equations and outline the model from Weller and Shahrokhi (2014). Section 4 analyses  
 102 the results from three advection tests, a test of a stably stratified atmosphere initially at rest, and  
 103 orographically induced gravity waves. Concluding remarks are made in section 5.

104 **2. Grids**

105 Here we describe the formulation of the terrain following grids and the method of cut cell grid  
 106 construction. The techniques presented are used to define the grids for the experiments in section 4.  
 107 Gal-Chen and Somerville (1975) proposed a basic terrain following (BTF) coordinate defined  
 108 as

$$z = (H - h) (z^*/H) + h \quad (1)$$

109 where, in two dimensions,  $z(x, z^*)$  is the physical height of the Cartesian coordinate surface at the  
 110 model level with transformed height  $z^*$ ,  $H$  is the height of the domain, and  $h(x)$  is the height of  
 111 the terrain surface. In this formulation  $z$  varies between  $h$  and  $H$  and  $z^*$  ranges from 0 to  $H$ . Using  
 112 this coordinate, the terrain's influence decays linearly with height but disappears only at the top of  
 113 the domain. An example is shown in figure 1a.

114 The smooth level vertical (SLEVE) coordinate proposed by Schär et al. (2002) achieves a more  
 115 regular TF grid in the middle and top of the domain than the BTF coordinate. The terrain height  
 116 is split into large-scale and small-scale components,  $h_1$  and  $h_2$ , such that  $h = h_1 + h_2$ , with each  
 117 component having a different exponential decay. The transformation is defined as

$$z = z^* + h_1 b_1 + h_2 b_2 \quad (2)$$

118 where the vertical decay functions are given by

$$b_i = \frac{\sinh((H/s_i)^n - (z^*/s_i)^n)}{\sinh(H/s_i)^n} \quad (3)$$

119 and  $s_1$  and  $s_2$  are the scale heights of large-scale and small-scale terrain respectively. The exponent  
120  $n$  was introduced by Leuenberger et al. (2010) in order to increase cell thickness in the layers  
121 nearest the ground, allowing longer timesteps. Leuenberger et al. (2010) found the exponent has  
122 an optimal value of  $n = 1.35$ . Choosing  $n = 1$  gives the decay functions used by Schär et al.  
123 (2002). An example of the SLEVE grid can be seen in figure 1b.

124 Most implementations of terrain following layers use a coordinate system that makes the com-  
125 putational domain rectangular, but introduces metric terms into the equations of motion. Instead,  
126 the model employed in this study uses Cartesian coordinates and non-orthogonal grids. By doing  
127 so, results from the same model can be compared between terrain following and cut cell grids  
128 without modifying the equation set or discretisation.

129 Cut cell grids are generated in a different way to the typical shaving technique described by  
130 Adcroft et al. (1997). Starting from a uniform grid, all cell vertices that lie beneath the orography  
131 are moved up to the surface. Additionally, to avoid creating very thin cells, all vertices up to  
132  $2\Delta z/5$  above the orography are moved down to the surface. Where all four of a cell's vertices are  
133 moved, the cell has zero volume and so it is removed. Where two vertices at the same horizontal  
134 location are moved up to the surface they will occupy the same point; this results in a zero-length  
135 edge that is removed to create a triangular cell. Figure 2 shows how a  $2 \times 3$ -cell, uniform grid is  
136 transformed into a cut cell grid. Cells  $c_5$  and  $c_6$  are removed because they have zero volume, and  
137 the zero-length edge at point  $q$  is removed to create a triangular cell,  $c_3$ . Point  $p$  is moved down  
138 because it is within  $2\Delta z/5$  of the surface, avoiding the creation of a very thin cell.

139 Some small cells are generated but, unlike most cut cell grids, cells are typically made smaller  
140 in height but their width is unaltered. A grid that has these thin cells can be seen in figure 5c. This  
141 technique has the advantage that cells are not shortened in the direction of flow and so there should  
142 be no additional constraints on the advective Courant number.

143 **3. Models**

144 Three models are used for the test cases in this study: two linear advection models and a model  
145 of the fully-compressible Euler equations. All are operated in a two-dimensional  $x-z$  slice config-  
146 uration.

147 The two finite volume models make use of the upwind-biased multidimensional cubic advection  
148 scheme from Weller and Shahrokhi (2014) which is non-monotonic and not flux corrected. The  
149 scheme uses a least-squares approach to fit a multidimensional polynomial over an upwind-biased  
150 stencil which contains more cells than the number of polynomial coefficients. This fit is used  
151 to interpolate cell values onto face values for discretisation of the advection term using Guass's  
152 divergence theorem. Following Lashley (2002) and Weller et al. (2009), the two cells either side  
153 of the face we are interpolating onto are weighted in the least squares fit so that the fit goes nearly  
154 exactly through these cell centres but does not go exactly through the other points. This method  
155 worked well when used for terrain following meshes by Weller and Shahrokhi (2014) but can be  
156 unstable in the presence of very small cut cells. This is because the least squares fit can generate a  
157 larger interpolation weight for the downwind cell than the upwind cell. In order to overcome this  
158 problem, wherever a large downwind cell interpolation weight is calculated by the least-squares  
159 fit, the weighting of the upwind cell is increased for the least-squares fitting and the fit is re-  
160 calculated. This procedure is repeated until the interpolation weight of the upwind cell is greater  
161 than the interpolation weight of the downwind cell. More details of this approach and a study of  
162 its behaviour is the subject of a future publication.

163 *a. Finite volume linear advection model*

164 The first model discretises the linear advection equation in flux form:

$$\partial\phi/\partial t + \nabla \cdot (\mathbf{u}\phi) = 0 \quad (4)$$

165 where  $\mathbf{u} = (u, w)$  is a prescribed velocity field and the tracer density,  $\phi$ , is interpolated onto cell  
 166 faces using one of two schemes: first, the centred linear scheme which takes the average of the two  
 167 neighbouring cell values; second, the upwind-biased cubic scheme. The time derivative is solved  
 168 using a three-stage, second order Runge-Kutta scheme defined as:

$$\phi^* = \phi^{(n)} + \Delta t f(\phi^{(n)}) \quad (5a)$$

$$\phi^{**} = \phi^{(n)} + \frac{\Delta t}{2} \left( f(\phi^{(n)}) + f(\phi^*) \right) \quad (5b)$$

$$\phi^{(n+1)} = \phi^{(n)} + \frac{\Delta t}{2} \left( f(\phi^{(n)}) + f(\phi^{**}) \right) \quad (5c)$$

169 where  $f(\phi^{(n)}) = -\nabla \cdot (\mathbf{u}\phi^{(n)})$  at time level  $n$ . This time-stepping scheme is used for consistency  
 170 with the trapezoidal implicit scheme used for the fully-compressible model, described in sec-  
 171 tion 3c. To ensure that the discrete velocity field is non-divergent, velocities are prescribed at cell  
 172 faces by differencing the streamfunction,  $\Psi(x, z)$ , along the edges from  $\Psi$  stored at cell vertices.

173 *b. Finite difference linear advection model*

174 The second model is a modified version of the linear advection model first used by Schär et al.  
 175 (2002). It uses terrain following coordinates and it is configured with leapfrog timestepping and  
 176 either second-order centred differences, or a fourth-order centred difference scheme given by:

$$\frac{\partial u\phi}{\partial x} \approx \frac{1}{\Delta x} \left( u_{i+\frac{1}{2}} F_{i+\frac{1}{2}} - u_{i-\frac{1}{2}} F_{i-\frac{1}{2}} \right) \quad (6a)$$

$$F_{i+\frac{1}{2}} = \frac{1}{12} (-\phi_{i+2} + 7\phi_{i+1} + 7\phi_i - \phi_{i-1}) \quad (6b)$$

177 and similarly for  $\partial(w\phi)/\partial z$ .

178 Once again, velocity fields are prescribed using a streamfunction defined at cell vertices (referred  
 179 to as double staggered grid points by Schär et al. (2002)). The original version of the code effec-  
 180 tively smoothed the orography, interpolating the geometric height,  $z$ , at doubly staggered points  
 181 from values at adjacent half levels in order to calculate the streamfunction. The modified version  
 182 used here directly calculates the height at vertices to enable comparisons with the finite volume  
 183 model solutions.

184 *c. Finite volume fully-compressible model*

185 The third model is taken from Weller and Shahrokhi (2014) which details a discretisation of the  
 186 fully-compressible Euler equations, given by

$$\text{Momentum} \quad \frac{\partial \rho \mathbf{u}}{\partial t} + \nabla \cdot \rho \mathbf{u} \otimes \mathbf{u} = \rho \mathbf{g} - c_p \rho \theta \nabla \Pi - \mu \rho \mathbf{u} \quad (7a)$$

$$\text{Continuity} \quad \frac{\partial \rho}{\partial t} + \nabla \cdot \rho \mathbf{u} = 0 \quad (7b)$$

$$\text{Thermodynamic equation} \quad \frac{\partial \rho \theta}{\partial t} + \nabla \cdot \rho \mathbf{u} \theta = 0 \quad (7c)$$

$$\text{Ideal gas law} \quad \Pi^{(1-\kappa)/\kappa} = \frac{R \rho \theta}{p_0} \quad (7d)$$

187 where  $\rho$  is the density,  $\mathbf{u}$  is the velocity field,  $\mathbf{g}$  is the gravitational acceleration,  $c_p$  is the heat  
 188 capacity at constant pressure,  $\theta = T (p_0/p)^\kappa$  is the potential temperature,  $T$  is the temperature,  
 189  $p$  is the pressure,  $p_0 = 1000 \text{ hPa}$  is a reference pressure,  $\Pi = (p/p_0)^\kappa$  is the Exner function of  
 190 pressure, and  $\kappa = R/c_p$  is the gas constant to heat capacity ratio.  $\mu$  is a damping function used for  
 191 the sponge layer in the gravity waves test in section 4d.

192 The fully-compressible model uses the C-grid staggering in the horizontal and the Lorenz stag-  
 193 gering in the vertical such that  $\theta$ ,  $\rho$  and  $\Pi$  are stored at cell centroids and the covariant component  
 194 of velocity at cell faces. The model is configured without Coriolis forces.

195     Acoustic and gravity waves are treated implicitly and advection is treated explicitly. The trape-  
196     zoidal implicit treatment of fast waves and the Hodge operator suitable for non-orthogonal grids  
197     are described in appendix A. To avoid time-splitting errors between the advection and the fast  
198     waves, the advection is time-stepped using a three-stage, second-order Runge-Kutta scheme. The  
199     advection terms of the momentum and  $\theta$  equations, (7a) and (7c), are discretised in flux form  
200     using the upwind-biased cubic scheme.

## 201     4. Results

202     A series of two-dimensional tests are performed over idealised orography. For each test, results  
203     on terrain following and cut cell grids are compared. The first test from Schär et al. (2002) advects  
204     a tracer in a horizontal velocity field. Second, a new tracer advection test is formulated employing  
205     a terrain following velocity field to challenge the advection scheme on cut cell grids. The third  
206     test solves the Euler equations for a stably stratified atmosphere initially at rest, following Klemp  
207     (2011). Fourth, as specified by Schär et al. (2002), a test of orographically-induced gravity waves  
208     is performed. Finally, another advection test is formulated that transports a stably stratified thermal  
209     profile in a terrain following velocity field. No explicit diffusion is used in any of the tests.

210     The OpenFOAM implementation of the numerical model, grid generation utilities and test  
211     cases are available at <https://github.com/hertzsprung/tf-cutcell-comparison/tree/shaw-weller-2015-mwr>.

### 213     a. *Horizontal advection*

214     Following Schär et al. (2002), a tracer is transported above wave-shaped terrain by solving the  
215     advection equation for a prescribed horizontal wind. This test challenges the accuracy of the  
216     advection scheme in the presence of grid distortions.

217 The domain width is 301 km, taken as the horizontal distance between the inlet and outlet bound-  
 218 aries. The domain is 25 km high, discretized onto a grid with  $\Delta x = 1$  km and  $\Delta z^* = 500$  m. Note  
 219 that Schär et al. (2002) measured the domain width as 300 km between the outermost cell centres  
 220 where tracer values are specified. Both formulations create a cell centre (or mass point) rather than  
 221 a cell face (or horizontal velocity point) over the top of the highest peak which is crucial for the  
 222 accuracy of the centred advection schemes.

223 The terrain is wave-shaped, specified by the surface height,  $h$ , such that

$$h(x) = h^* \cos^2(\alpha x) \quad (8a)$$

224 where

$$h^*(x) = \begin{cases} h_0 \cos^2(\beta x) & \text{if } |x| < a \\ 0 & \text{otherwise} \end{cases} \quad (8b)$$

225 where  $a = 25$  km is the mountain envelope half-width,  $h_0 = 3$  km is the maximum mountain height,  
 226  $\lambda = 8$  km is the wavelength,  $\alpha = \pi/\lambda$  and  $\beta = \pi/(2a)$ . On the SLEVE grid, the large-scale  
 227 component  $h_1$  is given by  $h_1(x) = h^*(x)/2$  and  $s_1 = 15$  km is the large scale height, and  $s_2 = 2.5$  km  
 228 is the small scale height. The optimisation of SLEVE by Leuenberger et al. (2010) is not used, so  
 229 the exponent  $n = 1$ .

230 The wind is entirely horizontal and is prescribed as

$$u(z) = u_0 \begin{cases} 1 & \text{if } z \geq z_2 \\ \sin^2 \left( \frac{\pi}{2} \frac{z-z_1}{z_2-z_1} \right) & \text{if } z_1 < z < z_2 \\ 0 & \text{otherwise} \end{cases} \quad (9)$$

231 where  $u_0 = 10$  m s<sup>-1</sup>,  $z_1 = 4$  km and  $z_2 = 5$  km. This results in a constant wind above  $z_2$ , and zero  
 232 flow at 4 km and below.

233 The discrete velocity field is defined using a streamfunction,  $\Psi$ . Given that  $u = -\partial\Psi/\partial z$ , the  
 234 streamfunction is found by vertical integration of the velocity profile:

$$\Psi(z) = -\frac{u_0}{2} \begin{cases} (2z - z_1 - z_2) & \text{if } z > z_2 \\ z - z_1 - \frac{z_2 - z_1}{\pi} \sin\left(\pi \frac{z - z_1}{z_2 - z_1}\right) & \text{if } z_1 < z \leq z_2 \\ 0 & \text{if } z \leq z_1 \end{cases} \quad (10)$$

235 A tracer with density  $\phi$  is positioned upstream above the height of the terrain. It has the shape

$$\phi(x, z) = \phi_0 \begin{cases} \cos^2\left(\frac{\pi r}{2}\right) & \text{if } r \leq 1 \\ 0 & \text{otherwise} \end{cases} \quad (11)$$

236 having radius,  $r$ , given by

$$r = \sqrt{\left(\frac{x - x_0}{A_x}\right)^2 + \left(\frac{z - z_0}{A_z}\right)^2} \quad (12)$$

237 where  $A_x = 25\text{ km}$ ,  $A_z = 3\text{ km}$  are the horizontal and vertical half-widths respectively, and  $\phi_0 =$   
 238  $1\text{ kg m}^{-3}$  is the maximum density of the tracer. At  $t = 0\text{ s}$ , the tracer is centred at  $(x_0, z_0) =$   
 239  $(-50\text{ km}, 9\text{ km})$  so that the tracer is upwind of the mountain and well above the maximum terrain  
 240 height of 3 km. Analytic solutions can be found by setting the tracer centre such that  $x_0 = ut$ . Tests  
 241 are integrated forward in time for 10000 s with a timestep of  $\Delta t = 25\text{ s}$ .

242 The test was executed on the BTF, SLEVE and cut cell grids using a centred linear scheme and  
 243 the upwind-biased cubic scheme. Results were also obtained on BTF and SLEVE grids with the  
 244 fourth order scheme from Schär et al. (2002) using the modified version of their code.

245 Minimum and maximum tracer values and  $\ell_2$  error norms on the BTF, SLEVE, cut cell and  
 246 regular grids are summarised in table 1, where the  $\ell_2$  error norm is defined as

$$\ell_2 = \sqrt{\frac{\sum_c (\phi - \phi_T)^2 \mathcal{V}_c}{\sum_c (\phi_T^2 \mathcal{V}_c)}} \quad (13)$$

247 where  $\phi$  is the numerical tracer value,  $\phi_T$  is the analytic value and  $\mathcal{V}_c$  is the cell volume.

248 The results of the cubic upwind-biased scheme on TF and regular grids are comparable with  
249 those for the fourth-order centred scheme from Schär et al. (2002). Error is largest on the BTF  
250 grid with  $\ell_2 = 0.112$  but is significantly reduced on the SLEVE grid with  $\ell_2 = 0.0146$ . Advection  
251 is most accurate on the cut cell grid, with  $\ell_2$  approximately half of that on the SLEVE grid. Tracer  
252 minima and maxima for the centred linear and fourth order schemes are lower than those presented  
253 by Schär et al. (2002) because no interpolation is used to calculate the streamfunction.

254 The results of the horizontal advection test show that numerical errors are due either to misalign-  
255 ment of the flow with the grid, or to grid distortions. In the following section, we propose a new  
256 test in order to identify the cause of the errors.

257 *b. Terrain following advection*

258 In the horizontal advection test, results were least accurate on the BTF grid, where the grid  
259 was most non-orthogonal and flow was misaligned with the grid layers. Here, we formulate a  
260 new tracer advection test in which the velocity field is everywhere tangential to the basic terrain  
261 following coordinate surfaces. On the BTF grid, the flow is then aligned with the grid, but the  
262 data in the multidimensional advection stencil is not uniformly distributed because the BTF grid  
263 is non-orthogonal. Conversely, on the cut cell grid, the flow is misaligned with the grid but, except  
264 in the lowest layer, the grid is orthogonal. This test determines whether the primary source of  
265 numerical error is due to non-orthogonality or misalignment of the flow with grid layers.

266 The spatial domain, mountain profile, initial tracer profile and discretisation are the same as  
267 those in the horizontal tracer advection test, except for the timestep  $\Delta t = 20$  s. The velocity field is  
268 defined using a streamfunction,  $\Psi$ , so that the discrete velocity field is non-divergent and follows

269 the BTF coordinate surfaces given by equation (1) such that

$$\Psi(x, z) = -u_0 H \frac{z - h}{H - h} \quad (14)$$

270 where  $u_0 = 10 \text{ m s}^{-1}$ , which is the horizontal wind speed where  $h(x) = 0$ . The horizontal and  
271 vertical components of velocity,  $u$  and  $w$ , are then given by

$$u = -\frac{\partial \Psi}{\partial z} = u_0 \frac{H}{H - h}, \quad w = \frac{\partial \Psi}{\partial x} = u_0 H \frac{dh}{dx} \frac{H - z}{(H - h)^2} \quad (15)$$

$$\frac{dh}{dx} = -h_0 [\beta \cos^2(\alpha x) \sin(2\beta x) + \alpha \cos^2(\beta x) \sin(2\alpha x)] \quad (16)$$

272 Unlike the horizontal advection test, flow extends from the top of the domain all the way to the  
273 ground. The discrete velocity field is calculated using the streamfunction in the same way as the  
274 horizontal advection test.

275 At  $t = 10000 \text{ s}$  the tracer has passed over the mountain. The horizontal position of the tracer  
276 centre can be calculated by integrating along the trajectory to find  $t$ , the time taken to pass from  
277 one side of the mountain to the other:

$$dt = dx/u(x) \quad (17)$$

$$t = \int_0^x \frac{H - h(x)}{u_0 H} dx \quad (18)$$

$$t = \frac{x}{u_0} - \frac{h_0}{16u_0 H} \left[ 4x + \frac{\sin 2(\alpha + \beta)x}{\alpha + \beta} + \frac{\sin 2(\alpha - \beta)x}{\alpha - \beta} + 2 \left( \frac{\sin 2\alpha x}{\alpha} + \frac{\sin 2\beta x}{\beta} \right) \right] \quad (19)$$

278 Hence, we find that  $x(t = 10000 \text{ s}) = 51577.4 \text{ m}$ . Because the velocity field is non-divergent,  
279 the flow accelerates over mountain ridges and the tracer travels 1577.4 m further compared to  
280 advection in the purely horizontal velocity field. Tracer height is unchanged downwind of the  
281 mountains because advection is parallel to the coordinate surfaces.

282 Tracer contours at  $t = 0 \text{ s}$ ,  $5000 \text{ s}$  and  $10000 \text{ s}$  are shown in Figure 3 using the centred linear  
283 scheme on the BTF grid and cut cell grid (3a and 3b respectively). At  $t = 5000 \text{ s}$ , the tracer is

284 distorted by the terrain-following velocity field. On the BTF grid, the tracer correctly returns to  
285 its original shape having cleared the mountain by  $t = 10000$  s, but this is not the case with centred  
286 linear scheme on the cut cell grid. Here, the tracer has spread vertically due to increased numerical  
287 errors when the tracer is transported between layers. Dispersion errors are apparent with grid-scale  
288 oscillations that travel in the opposite direction to the wind (figure 3d) and some artifacts remain  
289 above the mountain peak.

290 A small improvement is obtained on the BTF grid by using the upwind-biased cubic scheme: as  
291 seen in figure 3e, errors are less than 0.02 in magnitude and errors are confined to the expected  
292 region of the tracer. However, results are substantially improved by using the upwind-biased cubic  
293 scheme on the cut cell grid (figure 3f). Results on the SLEVE grid are comparable to those on the  
294 cut cell grid except that the artifacts above the mountain peak with the centred linear scheme on  
295 the cut cell grid are not present on the SLEVE grid (not shown).

296  $\ell_2$  errors and tracer extrema for this test are compared with the horizontal advection results in  
297 table 1. In the terrain following velocity field, tracer accuracy is greatest on the BTF grid. Errors  
298 are about ten times larger on the SLEVE and cut cell grids compared to the BTF grid.

299 We conclude from this test that accuracy depends upon alignment of the flow with the grid, and  
300 accuracy is not significantly reduced by grid distortions. Error on the BTF grid in the terrain fol-  
301 lowing advection test is comparable with the error on the SLEVE grid in the horizontal advection  
302 test.

303 *c. Stratified atmosphere initially at rest*

304 An idealised terrain profile is defined along with a stably stratified atmosphere at rest in hy-  
305 drostatic balance. The analytic solution is time-invariant, but numerical errors in calculating the  
306 pressure gradient can give rise to spurious velocities which become more severe over steeper ter-

307 rain (Klemp 2011). Cut cell grids are often suggested as a technique for reducing these spurious  
308 circulations (Yamazaki and Satomura 2010; Jebens et al. 2011; Good et al. 2014).

309 The test setup follows the specification by Klemp (2011). The domain is 200 km wide and 20 km  
310 high, and the grid resolution is  $\Delta x = \Delta z^* = 500$  m. All boundary conditions are no normal flow.

311 The wave-shaped mountain profile has a surface height,  $h$ , given by

$$h(x) = h_0 \exp\left(-\left(\frac{x}{a}\right)^2\right) \cos^2(\alpha x) \quad (20)$$

312 where  $a = 5$  km is the mountain half-width,  $h_0 = 1$  km is the maximum mountain height and  
313  $\lambda = 4$  km is the wavelength. For the optimised SLEVE grid, the large-scale component  $h_1$  is  
314 specified as

$$h_1(x) = \frac{1}{2} h_0 \exp\left(-\left(\frac{x}{a}\right)^2\right) \quad (21)$$

315 and, following Leuenberger et al. (2010),  $s_1 = 4$  km is the large scale height,  $s_2 = 1$  km is the small  
316 scale height, and the optimal exponent value of  $n = 1.35$  is used.

317 Tests were performed with two different stability profiles, both having an initial potential tem-  
318 perature field has  $\theta(z = 0) = 288$  K and a constant static stability with Brunt-Väisälä frequency  
319  $N = 0.01 \text{ s}^{-1}$  everywhere, except for a more stable layer of  $N = 0.02 \text{ s}^{-1}$ . Figure 4a shows  
320 where this inversion layer is positioned in the two tests: the ‘high inversion’ test follows Klemp  
321 (2011), placing the layer between  $2 \text{ km} \leq z \leq 3 \text{ km}$ ; the ‘low inversion’ test is designed to chal-  
322 lenge the pressure gradient calculations on the cut cell grid by placing the inversion layer between  
323  $0.5 \text{ km} \leq z \leq 1.5 \text{ km}$  so that it intersects the terrain.

324 The Exner function of pressure is calculated so that it is in discrete hydrostatic balance in the  
325 vertical direction (Weller and Shahrokhi 2014). The damping function,  $\mu$ , is set to  $0 \text{ s}^{-1}$ . Unlike  
326 Klemp (2011), there is no eddy diffusion in the equation set.

327 The test was integrated forward by 5 hours using a timestep  $\Delta t = 100\text{s}$  on the BTF, SLEVE  
328 and cut cell grids. Maximum vertical velocities are presented in figure 4b and are similar on  
329 the BTF, SLEVE and cut cell grids. For the high inversion test, the largest vertical velocity of  
330  $0.37\text{ m s}^{-1}$  was found on the BTF grid after 400 s, compared with a maximum of  $\sim 7\text{ m s}^{-1}$  found  
331 by Klemp (2011) using their improved horizontal pressure gradient formulation. Errors are two  
332 orders of magnitude smaller on the cut cell grid with vertical velocities of  $\sim 1 \times 10^{-4}\text{ m s}^{-1}$ , but  
333 this advantage is lost when the inversion layer is lowered to intersect the terrain. Unlike the result  
334 from Klemp (2011), the SLEVE grid does not further reduce vertical velocities compared to the  
335 BTF grid. This implies that the numerics we are using are less sensitive to grid distortions.

336 Good et al. (2014) found the maximum vertical velocity in their cut cell model was  
337  $1 \times 10^{-12}\text{ m s}^{-1}$ , which is better than any result obtained here. It is worth noting that our model  
338 stores values at the geometric centre of cut cells, whereas the model used by Good et al. (2014)  
339 has cell centres at the centre of the uncut cell, resulting in the centre of some cut cells being below  
340 the ground (S.-J. Lock 2014, personal communication). This means that the grid is effectively  
341 regular when calculating horizontal and vertical gradients. This would account for the very small  
342 velocities found by Good et al. (2014).

343 The results in figure 4b have maximum errors that are comparable with Weller and Shahrokhi  
344 (2014) but, due to the more stable split into implicitly and explicitly treated terms (described in  
345 the appendix), the errors decay over time due to the dissipative nature of the advection scheme.

346 In summary, we reproduce the result found by Good et al. (2014) that cut cells can reduce  
347 spurious velocities over orography. However, in addition, we find that, with the right numerics,  
348 these errors can be very small on a BTF grid. We also find that, if changes in stratification intersect  
349 cut cells, spurious velocities on cut cell grids are comparable with those on TF grids.

350 *d. Gravity waves*

351 The test originally specified by Schär et al. (2002) prescribes flow over terrain with small-scale  
352 and large-scale undulations which induces propagating and evanescent gravity waves.

353 Following Melvin et al. (2010), the domain is 300 km wide and 30 km high. The mountain  
354 profile has the same form as equation (20), but the gravity waves tests have a mountain height of  
355  $h_0 = 250$  m. As in the resting atmosphere test,  $a = 5$  km is the mountain half-width and  $\lambda = 4$  km  
356 is the wavelength.

357 A uniform horizontal wind  $(u, w) = (10, 0)$  m s<sup>-1</sup> is prescribed in the interior domain and at the  
358 inlet boundary. No normal flow is imposed at the top and bottom boundaries and the velocity field  
359 has a zero gradient outlet boundary condition.

360 The initial thermodynamic conditions have constant static stability with  $N = 0.01$  s<sup>-1</sup> every-  
361 where, such that

$$\theta(z) = \theta_0 \exp\left(\frac{N^2}{g} z\right) \quad (22)$$

362 where the temperature at  $z = 0$  is  $\theta_0 = 288$  K. Potential temperature values are prescribed at the  
363 inlet and upper boundary using equation (22), and a zero gradient boundary condition is applied at  
364 the outlet. At the ground, fixed gradients are imposed by calculating the component of  $\nabla\theta$  normal  
365 to each face using the vertical derivative of equation (22). For the Exner function of pressure,  
366 hydrostatic balance is prescribed on top and bottom boundaries and the inlet and outlet are zero  
367 normal gradient.

368 Sponge layers are added to the upper 10 km and leftmost 10 km at the inlet boundary to damp  
 369 the reflection of waves. The damping function,  $\mu$ , is adapted from Melvin et al. (2010) such that

$$\mu(x, z) = \mu_{\text{upper}} + \mu_{\text{inlet}} \quad (23)$$

$$\mu_{\text{upper}}(z) = \begin{cases} \bar{\mu} \sin^2 \left( \frac{\pi}{2} \frac{z - z_B}{H - z_B} \right) & \text{if } z \geq z_B \\ 0 & \text{otherwise} \end{cases} \quad (24)$$

$$\mu_{\text{inlet}}(x) = \begin{cases} \bar{\mu} \sin^2 \left( \frac{\pi}{2} \frac{x_I - x}{x_I - x_0} \right) & \text{if } x < x_I \\ 0 & \text{otherwise} \end{cases} \quad (25)$$

370 where  $\bar{\mu} = 1.2 \text{ s}^{-1}$  is the damping coefficient,  $z_B = 20 \text{ km}$  is the bottom of the sponge layer,  $H =$   
 371  $30 \text{ km}$  is the top of the domain,  $x_0 = -150 \text{ km}$  is the leftmost limit of the domain and  $x_I = -140 \text{ km}$   
 372 is the rightmost extent of the inlet sponge layer. The sponge layer is only active on faces whose  
 373 normal is vertical so that it damps vertical momentum only.

374 Note that, while the domain itself is 30 km in height, for the purposes of generating BTF grids,  
 375 the domain height is set to 20 km because the sponge layer occupies the uppermost 10 km.

376 The simulation is integrated forward by 5 hours and the timestep,  $\Delta t = 8\Delta z/300 \text{ s}$ , is chosen  
 377 so that it scales linearly with spatial resolution and, following the original test specified by Schär  
 378 et al. (2002),  $\Delta t = 8 \text{ s}$  when  $\Delta z = 300 \text{ m}$ . Test results are compared between the BTF and cut cell  
 379 grids at several resolutions. The spatial and temporal resolutions tested are shown in table 2. The  
 380 lowest resolution is the same as that used by Schär et al. (2002), and higher resolutions preserve  
 381 the same aspect ratio. The vertical resolution is chosen to test various configurations of cut cell  
 382 grid. At  $\Delta z = 300 \text{ m}$ , the mountain lies entirely within the lowest layer of cells, while at  $\Delta z = 250 \text{ m}$   
 383 and  $\Delta z = 125 \text{ m}$  the mountain peak is aligned with the interface between layers. With increasing  
 384 resolutions up to  $\Delta z = 50 \text{ m}$ , the orography intersects more layers and becomes better resolved.

385 Three of the cut cell grids are shown in figure 5 at  $\Delta z = 300\text{ m}$ ,  $200\text{ m}$  and  $150\text{ m}$ . Small cells are  
386 visible on the  $150\text{ m}$  grid but, on the  $200\text{ m}$  grid, the small cells are merged with those in the layer  
387 above.

388 The ratio of minimum and maximum cell areas in the various grids is shown in table 3, providing  
389 an indication of size of the smallest cut cells. As expected, there is almost no variation in cell sizes  
390 on the BTF grids. Small cells are generated on cut cell grids at resolutions finer than  $\Delta z = 300\text{ m}$   
391 in which the terrain intersects grid layers.

392 At  $\Delta z = 300\text{ m}$ , vertical velocities on the BTF and cut cell grids are visually indistinguishable  
393 (not shown). They agree with the high resolution mass-conserving semi-implicit semi-Lagrangian  
394 solution from Melvin et al. (2010). The initial thermal profile is subtracted from the potential  
395 temperature field at the end of the integration to reveal the structure of thermal anomalies. The  
396 anomalies on the BTF grid with  $\Delta z = 50\text{ m}$  is shown in figure 6. A vertical profile is taken at  $x =$   
397  $50\text{ km}$ , marked by the dashed line in figure 6, with results shown for the BTF grids in figure 7a and  
398 on the cut cell grids in figure 7b. The position is chosen to be far away from the mountain where the  
399 gravity wave amplitude is small in order to better reveal numerical errors. On all grids, potential  
400 temperature differences increase with height in the lowest  $1200\text{ m}$  at  $x = 50\text{ km}$ , in agreement with  
401 the results seen in figure 6. Results are seen to converge on all grids, with the exception of small  
402 errors in the lowest layers on the cut cell grids.

403 To summarize, results of the gravity waves test on all grids are in good agreement with the  
404 reference solution from Melvin et al. (2010). The potential temperature field converges, though  
405 errors are found in the lowest layers on the cut cell grids. The source of the errors in the cut cell  
406 grids will be investigated further with an advection test in the following subsection.

407 *e. Terrain following advection of thermal profile*

408 The potential temperature anomalies in the gravity waves test do not converge with resolution  
 409 when using the cut cell grids. This may be due to differences in the wind fields between grids,  
 410 or errors in the advection of potential temperature, amongst other possible causes. To help estab-  
 411 lish the primary source of error, a new advection test is formulated in which the initial potential  
 412 temperature field from the gravity waves test is used. To eliminate any differences in wind fields,  
 413 the field is advected in a fixed, terrain-following velocity field that mimics the flow in the gravity  
 414 waves test.

415 The spatial domain, mountain profile, grid resolutions and timesteps are the same as those in the  
 416 gravity waves test in section 4d. The terrain following velocity field is defined by the streamfunc-  
 417 tion:

$$\Psi(x, z) = -u_0 \begin{cases} H_{\text{TF}} \frac{z-h}{H_{\text{TF}}-h} & \text{if } z \leq H_{\text{TF}} \\ z & \text{if } z > H_{\text{TF}} \end{cases} \quad (26)$$

418 where  $H_{\text{TF}} = 20\text{km}$  is the level at which the terrain following layers become flat; the domain  
 419 height is  $30\text{km}$ . For  $z \leq H_{\text{TF}}$ , the  $u$  and  $w$  components of velocity are given by equation (15), but  
 420  $h(x)$  has the same form as equation (20), hence the derivative is:

$$\frac{dh}{dx} = -h_0 \exp\left(-\left(\frac{x}{a}\right)^2\right) \left[ \alpha \sin(2\alpha x) - \frac{2x}{a^2} \cos^2(\alpha x) \right] \quad (27)$$

421 For  $z > H_{\text{TF}}$ ,  $u = u_0$  and  $w = 0$ .

422 The potential temperature field,  $\theta$ , and its boundary conditions, are the same as those of the  
 423 initial potential temperature field in the gravity waves test. Following the gravity waves test,  
 424 the simulation is integrated forward by  $18\,000\text{s}$ , by which time the potential temperature initially  
 425 upwind of the mountain will have cleared the mountain range. Hence, the analytic solution,  $\theta_T$ , can  
 426 be found by considering the vertical displacement of the thermal profile by the terrain following

427 velocity field:

$$\theta_T(x, z) = \theta_0 \exp\left(\frac{N^2}{g} z^*(x, z)\right) \quad (28)$$

428 where the potential temperature at  $z = 0$ ,  $\theta_0 = 288\text{K}$ , and the transform,  $z^*$ , is given by rearranging  
429 equation (1).

430 Enlargements of the error field near the mountain are shown in figure 8 at  $\Delta z = 50\text{m}$  with  
431 contours of potential temperature overlayed. Errors are only just visible on the BTF grid with  
432 an  $\ell_2$  error of  $1.12 \times 10^{-7}$ . However, on the cut cell grid, the error is about ten times larger.  
433 Advection errors are apparent around mountainous terrain, with small cells having some of the  
434 largest errors. These errors are advected horizontally along the lee slope, forming stripes. The  
435 same error structure is present on all cut cell grids.

436 For comparison with the potential temperature anomalies in the gravity waves test, vertical pro-  
437 files of potential temperature error are taken at  $x = 50\text{km}$ . As seen in figure 7c, errors are negligible  
438 on the BTF grids, but figure 7d reveals significant errors in the lowest layers of the cut cell grids  
439 that were advected from the mountain peaks.

440 While the magnitude and structure of error on the cut cell grids in this test differs from potential  
441 temperature anomalies in the gravity waves test, results on the BTF grids are in close agreement in  
442 both tests but not on the cut cell grids. Therefore, it is likely that anomalies on the cut cell grids in  
443 the gravity waves test are primarily due to errors in the advection of potential temperature through  
444 cut cells.

445 **5. Conclusions**

446 We have presented a like-for-like comparison between terrain following and cut cell grids using  
447 a single model. Accuracy on the BTF, SLEVE and cut cell grids was evaluated in a series of  
448 two-dimensional tests.

449 Across all tests, a high degree of accuracy was achieved for all grids. Even on the highly-  
450 distorted BTF grid errors were often small in the tests presented here. In the first two tests, tracers  
451 were advected by horizontal and terrain following velocity fields. We found that the accuracy of  
452 the upwind-biased cubic advection scheme depended upon alignment of the flow with the grid  
453 rather than on grid distortions. Spurious vertical velocities in the resting atmosphere tests were  
454 similar on terrain following and cut cell grids. In the gravity waves test, vertical velocities were in  
455 good agreement with the reference solution from Melvin et al. (2010) across all grids.

456 Cut cell grids reduced errors in the horizontal advection test. Conversely, in the terrain following  
457 tracer advection test, errors were large on the SLEVE and cut cell grids where velocities were  
458 misaligned with the grids. Errors were also large on the cut cell grids in the terrain following  
459 thermal advection test. This result suggests that, in the gravity waves test, potential temperature  
460 errors in the cut cell grids are primarily due to advection errors.

461 The cubic upwind-biased advection scheme takes an approach for treating small cut cells that  
462 differs from other existing approaches by adjusting weightings to ensure that advection remains  
463 upwind-biased near small cells. The implementation of this technique in OpenFOAM is available  
464 at <https://github.com/hertzsprung/AtmosFOAM/tree/shaw-weller-2015-mwr> and will  
465 be described in greater detail a future publication. Combined with semi-implicit timestepping and  
466 a new cut cell generation technique that preserves cell length in the direction of the flow, small cells  
467 did not impose additional timestep constraints. By using a suitable multidimensional advection

468 scheme and a curl-free pressure gradient formulation, we did not find significant advantages of  
 469 cut cells or smoothed coordinate systems unlike Good et al. (2014); Klemp (2011); Schär et al.  
 470 (2002). In contrast, errors that do not reduce with resolution are on cut cell grids. No significant  
 471 problems were found when using basic terrain following grids.

472 *Acknowledgments.* I am grateful to my co-supervisors John Methven and Terry Davies for their  
 473 valuable input, and to Christoph Schär (ETH) for his assistance in reproducing his advection test  
 474 results. The authors thank the two anonymous reviewers whose comments greatly improved this  
 475 manuscript. I am thankful for the NERC studentship which helped fund this work. Weller is  
 476 funded by NERC grant NE/H015698/1.

477 **Appendix A . Semi-implicit treatment of the Hodge operator**

478 In order to ensure curl-free pressure gradients, following Weller and Shahrokhi (2014), the co-  
 479 variant momentum component, that is the momentum at the cell face in the direction between cell  
 480 centres, is used as the prognostic variable for velocity:

$$481 \quad V_f = \rho_f \mathbf{u}_f \cdot \mathbf{d}_f \quad (29)$$

482 where  $\mathbf{d}_f$  is the vector between cell centres and subscript  $f$  means “at face  $f$ ”. The contravariant  
 483 momentum component, that is the flux across faces, is a diagnostic variable:

$$484 \quad U_f = \rho_f \mathbf{u}_f \cdot \mathbf{S}_f \quad (30)$$

485 where  $\mathbf{S}_f$  is the outward-pointing normal vector to face  $f$  with magnitude equal to the area of the  
 486 face. If  $U$  is the vector of all values of  $U_f$  and  $V$  is the vector of all values of  $V_f$  then we can define  
 487 the Hodge operator as a matrix that transforms  $V$  to  $U$ :

$$488 \quad U = HV. \quad (31)$$

486 For energy conservation, Thuburn and Cotter (2012) showed that the Hodge operator must be  
 487 symmetric and positive definite. We define a symmetric  $H$  suitable for arbitrary 3D meshes:

$$U_f = (\rho \mathbf{u})_F \cdot \mathbf{S}_f \quad (32)$$

488 where subscript  $F$  denotes mid-point interpolation from two surrounding cell values onto face  $f$ :

$$(\rho \mathbf{u})_F = \frac{1}{2} \sum_{c \in f} (\rho \mathbf{u})_C \quad (33)$$

489 where  $c \in f$  denotes the two cells sharing face  $f$ .  $(\rho \mathbf{u})_C$  is the consistent cell centre reconstruction  
 490 of  $\rho \mathbf{u}$  from surrounding values of  $V_f$ :

$$(\rho \mathbf{u})_C = \left( \sum_{f' \in c} \mathbf{d}_{f'} \otimes \mathbf{d}_{f'}^T \right)^{-1} \sum_{f' \in c} \mathbf{d}_{f'} V_{f'}$$

491 where  $\mathbf{d}_{f'} \otimes \mathbf{d}_{f'}^T$  is a  $3 \times 3$  tensor and so the inversion of the tensor sum is a local operation which  
 492 can be calculated once for every cell in the grid before time-stepping begins. The  $H$  implied  
 493 by this reconstruction of  $U$  is likely to be positive definite for meshes with sufficiently low non-  
 494 orthogonality, although this has not been proved.

495 The semi-implicit technique involves combining the momentum (7a), continuity (7b) and  $\theta$  (7c)  
 496 equations and the equation of state (7d) to form a Helmholtz equation to be solved implicitly, as  
 497 described by Weller and Shahrokhi (2014). The semi-implicit solution technique with a Hodge  
 498 operator can be defined by considering only a discretised form of the continuity equation:

$$\frac{\phi^{(n+1)} - \rho^{(n)}}{\Delta t} + \frac{1}{2} \left\{ \nabla \cdot (HV)^{(n)} + \nabla \cdot (HV)^{(n+1)} \right\} = 0. \quad (34)$$

499 The divergence is discretised using Gauss' divergence theorem so that:

$$\nabla \cdot (HV) = \frac{1}{\mathcal{V}_c} \sum_{f \in c} n_f (HV)_f \quad (35)$$

500 where  $\mathcal{V}_c$  is the volume of cell  $c$ ,  $f \in c$  denotes the faces of cell  $c$ , and  $n_f = 1$  if  $\mathbf{d}_f$  points outwards  
 501 from the cell and  $n_f = -1$  otherwise. Equation (35) is now a sum over a sum since  $(HV)_f$  is

502 one element of a matrix-vector multiply. In order to simplify the construction of the matrix for  
 503 the Helmholtz problem, only the diagonal terms of  $HV$  are treated implicitly. Therefore,  $H$  is  
 504 separated into a diagonal and off-diagonal matrix:

$$H = H_d + H_{off}. \quad (36)$$

505 Equation (34) can now be approximated by:

$$\frac{\phi^{(n+1)} - \rho^{(n)}}{\Delta t} + \frac{1}{2} \left\{ \nabla \cdot (HV)^{(n)} + \nabla \cdot (H_d V)^{(n+1)} + \nabla \cdot (H_{off} V)^\ell \right\} = 0 \quad (37)$$

506 where superscript  $\ell$  denotes lagged values taken from a previous iteration or from a previous stage  
 507 of a Runge-Kutta scheme. This was the approach taken by Weller and Shahrokhi (2014). However,  
 508 the numerical solution of equation (37) turns out to be unstable when using a large time-step on  
 509 highly non-orthogonal meshes associated with terrain following layers over steep orography. Im-  
 510 proved stability and energy conservation can be achieved by splitting  $H$  into a diagonal component  
 511 which would be correct on an orthogonal grid and a non-orthogonal correction:

$$H = H_c + H_{corr} \quad (38)$$

512 where the diagonal matrix  $H_c = |\mathbf{S}_f|/|\mathbf{d}_f|$  and the non-orthogonal correction is  $H_{corr} = H - H_c$ .

513 The orthogonal part,  $H_c$ , can be treated implicitly in the Helmholtz equation:

$$\frac{\phi^{(n+1)} - \rho^{(n)}}{\Delta t} + \frac{1}{2} \left\{ \nabla \cdot (HV)^{(n)} + \nabla \cdot (H_c V)^{(n+1)} + \nabla \cdot (H_{corr} V)^\ell \right\} = 0. \quad (39)$$

514 This form is used for the solutions of the Euler equations in this paper and is stable, with good  
 515 energy conservation for all of the tests presented.

## 516 References

517 Adcroft, A., C. Hill, and J. Marshall, 1997: Representation of topography by shaved cells in a  
 518 height coordinate ocean model. *Mon. Wea. Rev.*, **125**, 2293–2315.

519 Fast, J. D., 2003: Forecasts of valley circulations using the terrain-following and step-mountain  
520 vertical coordinates in the Meso-Eta model. *Wea. Forecasting*, **18**, 1192–1206.

521 Gal-Chen, T., and R. C. Somerville, 1975: On the use of a coordinate transformation for the  
522 solution of the Navier-Stokes equations. *J. Comp. Phys.*, **17**, 209–228.

523 Gallus, W. A., and J. B. Klemp, 2000: Behavior of flow over step orography. *Mon. Wea. Rev.*, **128**,  
524 1153–1164.

525 Gary, J. M., 1973: Estimate of truncation error in transformed coordinate, primitive equation  
526 atmospheric models. *J. Atmos. Sci.*, **30**, 223–233.

527 Good, B., A. Gadian, S.-J. Lock, and A. Ross, 2014: Performance of the cut-cell method of  
528 representing orography in idealized simulations. *Atmos. Sci. Lett.*, **15**, 44–49.

529 Jebens, S., O. Knoth, and R. Weiner, 2011: Partially implicit peer methods for the compressible  
530 Euler equations. *J. Comp. Phys.*, **230**, 4955–4974.

531 Klein, R., K. Bates, and N. Nikiforakis, 2009: Well-balanced compressible cut-cell simulation of  
532 atmospheric flow. *Philos. Trans. Roy. Soc. London*, **367**, 4559–4575.

533 Klemp, J. B., 2011: A terrain-following coordinate with smoothed coordinate surfaces. *Mon. Wea.*  
534 *Rev.*, **139**, 2163–2169.

535 Lashley, R. K., 2002: Automatic generation of accurate advection schemes on unstructured grids  
536 and their application to meteorological problems. Ph.D. thesis, University of Reading, 247 pp.,  
537 [Available online at <http://ethos.bl.uk/OrderDetails.do?uin=uk.bl.ethos.394176>].

538 Leuenberger, D., M. Koller, O. Fuhrer, and C. Schär, 2010: A generalization of the SLEVE vertical  
539 coordinate. *Mon. Wea. Rev.*, **138**, 3683–3689.

540 Melvin, T., M. Dubal, N. Wood, A. Staniforth, and M. Zerroukat, 2010: An inherently  
541 mass-conserving iterative semi-implicit semi-Lagrangian discretization of the non-hydrostatic  
542 vertical-slice equations. *Quart. J. Roy. Meteor. Soc.*, **136**, 799–814.

543 Mesinger, F., Z. I. Janjić, S. Ničkovic, D. Gavrilov, and D. G. Deaven, 1988: The step-mountain  
544 coordinate: Model description and performance for cases of alpine lee cyclogenesis and for a  
545 case of an Appalachian redevelopment. *Mon. Wea. Rev.*, **116**, 1493–1518.

546 Mesinger, F., and Coauthors, 2012: An upgraded version of the Eta model. *Meteor. Atmos. Phys.*,  
547 **116**, 63–79.

548 Schär, C., D. Leuenberger, O. Fuhrer, D. Lüthi, and C. Girard, 2002: A new terrain-following  
549 vertical coordinate formulation for atmospheric prediction models. *Mon. Wea. Rev.*, **130**, 2459–  
550 2480.

551 Simon, J. S., K. A. Lundquist, and F. K. Chow, 2012: Application of the immersed boundary  
552 method to simulations of flow over steep, mountainous terrain. *15th Conf. on Mountain Met.*,  
553 Steamboat, CO.

554 Steppeler, J., H.-W. Bitzer, M. Minotte, and L. Bonaventura, 2002: Nonhydrostatic atmospheric  
555 modeling using a  $z$ -coordinate representation. *Mon. Wea. Rev.*, **130**, 2143–2149.

556 Steppeler, J., R. Hess, U. Schättler, and L. Bonaventura, 2003: Review of numerical methods for  
557 nonhydrostatic weather prediction models. *Meteor. Atmos. Phys.*, **82**, 287–301.

558 Steppeler, J., S.-H. Park, and A. Dobler, 2013: Forecasts covering one month using a cut-cell  
559 model. *Geosci. Model Dev.*, **6**, 875–882.

560 Thuburn, J., and C. Cotter, 2012: A framework for mimetic discretization of the rotating shallow-  
561 water equations on arbitrary polygonal grids. *SIAM J. Sci. Comp.*, **34** (3), B203–B225.

562 Webster, S., A. Brown, D. Cameron, and C. Jones, 2003: Improvements to the representation of  
563 orography in the Met Office Unified Model. *Quart. J. Roy. Meteor. Soc.*, **129**, 1989–2010.

564 Weller, H., and A. Shahrokhi, 2014: Curl free pressure gradients over orography in a solution of  
565 the fully compressible Euler equations with implicit treatment of acoustic and gravity waves.  
566 *Mon. Wea. Rev.*, **142**, 4439–4457.

567 Weller, H., H. G. Weller, and A. Fournier, 2009: Voronoi, Delaunay, and block-structured mesh  
568 refinement for solution of the shallow-water equations on the sphere. *Mon. Wea. Rev.*, **137**,  
569 4208–4224.

570 Yamazaki, H., and T. Satomura, 2010: Nonhydrostatic atmospheric modeling using a combined  
571 Cartesian grid. *Mon. Wea. Rev.*, **138**, 3932–3945.

572 Zängl, G., 2012: Extending the numerical stability limit of terrain-following coordinate models  
573 over steep slopes. *Mon. Wea. Rev.*, **140**, 3722–3733.

574 **LIST OF TABLES**

575	<b>Table 1.</b> Minimum and maximum tracer densities ( $\text{kg m}^{-3}$ ) and $\ell_2$ error norms, defined	
576	by equation (13), at $t = 10000$ s in the horizontal and terrain following tracer	
577	advection tests using centred linear and cubic upwind-biased schemes. For the	
578	horizontal advection test, $\ell_2$ error norms, minimum and maximum values are	
579	given for the fourth order scheme using the modified code from Schär et al.	
580	(2002). . . . .	32
581	<b>Table 2.</b> Spatial and temporal resolutions used in the gravity waves test. The resolution	
582	of $\Delta z = 300$ m has the same parameters as the original test case specified by	
583	Schär et al. (2002). At other resolutions, the vertical resolution is prescribed,	
584	and horizontal and temporal resolutions are calculated to preserve the same	
585	aspect ratio as the original test case. . . . .	33
586	<b>Table 3.</b> Cell area ratios of BTF and cut cell grids used in the gravity waves and thermal	
587	advection tests. Cell sizes are almost uniform on BTF grids, but for the cut cell	
588	grids the cell area ratio gives an indication of the smallest cell sizes. . . . .	34

589 TABLE 1. Minimum and maximum tracer densities ( $\text{kg m}^{-3}$ ) and  $\ell_2$  error norms, defined by equation (13), at  
 590  $t = 10000$  s in the horizontal and terrain following tracer advection tests using centred linear and cubic upwind-  
 591 biased schemes. For the horizontal advection test,  $\ell_2$  error norms, minimum and maximum values are given for  
 592 the fourth order scheme using the modified code from Schär et al. (2002).

			Analytic	BTF	SLEVE	Cut cell	No terrain
Horizontal	Centred linear	$\ell_2$ error	0	0.284	0.0316	0.0304	0.0304
		min	0	-0.275	-0.0252	-0.0251	-0.0251
		max	1	0.925	0.985	0.985	0.985
	Fourth order	$\ell_2$ error	0	0.0938	0.00244	—	0.00234
		min	0	-0.0926	-0.00174	—	-0.00178
		max	1	1.00	0.984	—	0.983
	Cubic upwind-biased	$\ell_2$ error	0	0.112	0.0146	0.00784	0.00784
		min	0	-0.0464	-0.0106	-0.00674	-0.00674
		max	1	0.922	0.982	0.983	0.983
Terrain following	Centred linear	$\ell_2$ error	0	0.0338	0.235	0.374	—
		min	0	-0.0242	-0.120	-1.26	—
		max	1	0.984	0.950	1.11	—
	Cubic upwind-biased	$\ell_2$ error	0	0.0207	0.162	0.181	—
		min	0	-0.0109	-0.0263	-0.0284	—
		max	1	0.983	0.865	0.851	—

593 TABLE 2. Spatial and temporal resolutions used in the gravity waves test. The resolution of  $\Delta z = 300\text{ m}$  has  
 594 the same parameters as the original test case specified by Schär et al. (2002). At other resolutions, the vertical  
 595 resolution is prescribed, and horizontal and temporal resolutions are calculated to preserve the same aspect ratio  
 596 as the original test case.

$\Delta z$ (m)	$\Delta x$ (m)	$\Delta t$ (s)
500	833.3	13.33
300	500	8
250	416.7	6.667
200	333.3	5.333
150	250	4
125	208.3	3.333
100	166.7	2.667
75	125	2
50	83.33	1.333

597 TABLE 3. Cell area ratios of BTF and cut cell grids used in the gravity waves and thermal advection tests.  
 598 Cell sizes are almost uniform on BTF grids, but for the cut cell grids the cell area ratio gives an indication of the  
 599 smallest cell sizes.

$\Delta z$ (m)	max/min cell area ratio	
	BTF	Cut cell
500	1.01	1.68
300	1.01	4.11
250	1.01	3.52
200	1.01	6.04
150	1.01	6.46
125	1.01	6.12
100	1.01	6.22
75	1.01	5.98
50	1.01	6.29

## 600 LIST OF FIGURES

601 **Fig. 1.** Examples of (a) BTF, (b) SLEVE, and (c) a cut cell grid, showing cell edges in the lowest  
 602 four layers. The full two dimensional grids are 20 km wide and 20 km high. SLEVE param-  
 603 eters are specified in the resting atmosphere test in section 4c. The cut cell grid was created  
 604 by intersecting the terrain surface with a regular grid as described in section 2. Axes are in  
 605 units of m. . . . .

606 **Fig. 2.** Illustration of a cut cell grid (a) before, and (b) after construction. The terrain surface,  
 607 denoted by a heavy dotted line, intersects a uniform rectangular grid comprising six cells,  
 608  $c_1, \dots, c_6$ . The cell vertices, marked by open circles, are moved to the points at which the  
 609 terrain intersects vertical cell edges, marked by filled circles. Cells that have no volume are  
 610 removed. Where a cell has two vertices occupying the same point, the zero-length edge that  
 611 joins those vertices is removed. In this illustration, cells  $c_5$  and  $c_6$  are removed because they  
 612 have no volume, and the zero-length edge at point  $q$  is removed to create a triangular cell,  
 613  $c_4$ . Point  $p$  is moved down because it is within  $2\Delta z/5$  of the surface, avoiding the creation  
 614 of a thin cell. . . . .

615 **Fig. 3.** Tracer contours advected in a terrain following velocity field at  $t = 0$  s, 5000 s and 10 000 s  
 616 using the centred linear scheme on (a) the BTF grid, and (b) the cut cell grid with contour  
 617 intervals every 0.1. Errors at  $t = 10000$  s are shown for (c) the the centred linear scheme on  
 618 the BTF grid, (d) the centred linear scheme on the cut cell grid, (e) the upwind-biased cubic  
 619 scheme on the BTF grid, and (f) the upwind-biased cubic scheme on the cut cell grid with  
 620 contour intervals every 0.01. Negative contours denoted by dotted lines. The terrain profile  
 621 is also shown immediately above the  $x$  axis. . . . .

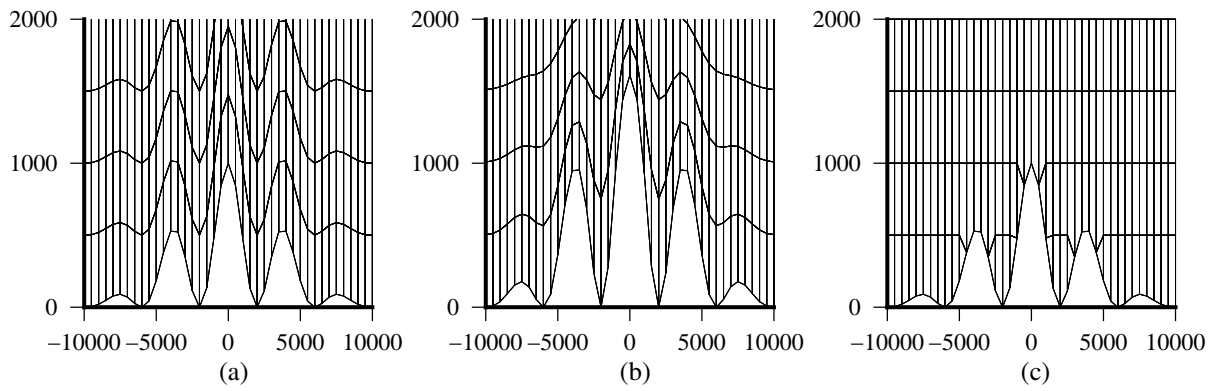
622 **Fig. 4.** Setup and results of a stratified atmosphere initially at rest. Tests are performed on four  
 623 grids for two different stability profiles, with panel (a) showing the placement of the inver-  
 624 sion layer in the two profiles. The low inversion is positioned so that it intersects the terrain,  
 625 shown immediately above the  $x$  axis. In each test, the inversion layer has a Brunt-Väisälä  
 626 frequency  $N = 0.02 \text{ s}^{-1}$ , and  $N = 0.01 \text{ s}^{-1}$  elsewhere. Panel (b) shows the maximum mag-  
 627 nitude of spurious vertical velocity,  $w$  ( $\text{m s}^{-1}$ ), with results on BTF, SLEVE, cut cell and  
 628 regular grids using the model from Weller and Shahrokh (2014) which includes a curl-free  
 629 pressure gradient formulation. Results for the high inversion test are shown with solid lines,  
 630 the low inversion test with dashed lines. . . . .

631 **Fig. 5.** Cut cell grids used for the gravity waves and thermal advection tests at (a)  $\Delta z = 300$  m,  
 632 (b)  $\Delta z = 200$  m, and (c)  $\Delta z = 150$  m. The mountain peak  $h_0 = 250$  m. At  $\Delta z = 300$  m and  
 633  $\Delta z = 200$  m, the grid creation process has merged small cells with the cells in the layer  
 634 above but, at  $\Delta z = 150$  m, small cells have been retained. The full two dimensional grids are  
 635 300 km wide and 30 km high. Axes are in units of m. . . . .

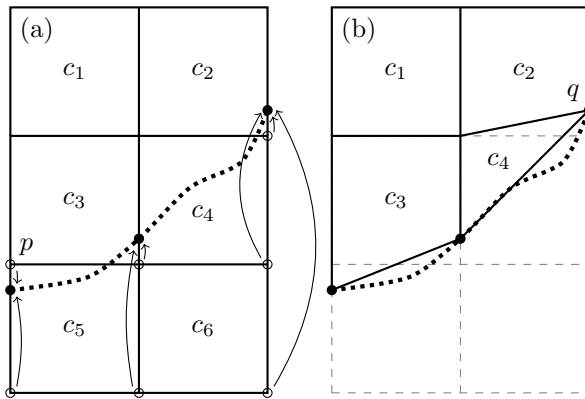
636 **Fig. 6.** Differences in potential temperature between the start and end of the gravity waves test on  
 637 the BTF grid with  $\Delta z = 50$  m. The dashed line at  $x = 50$  km marks the position of the vertical  
 638 profile in figure 7. Axes are in units of m. . . . .

639 **Fig. 7.** Vertical profiles of potential temperature differences between the start and end of the gravity  
 640 waves test on (a) the BTF grid, and (b) the cut cell grid. Results are compared with thermal  
 641 advection tests results, showing differences in potential temperature between the numeric  
 642 and analytic solutions at  $t = 18000$  s on (c) the BTF grid, and (d) the cut cell grid. The  
 643 results are convergent, except for errors found in the lowest layers on the cut cell grids. . . . .

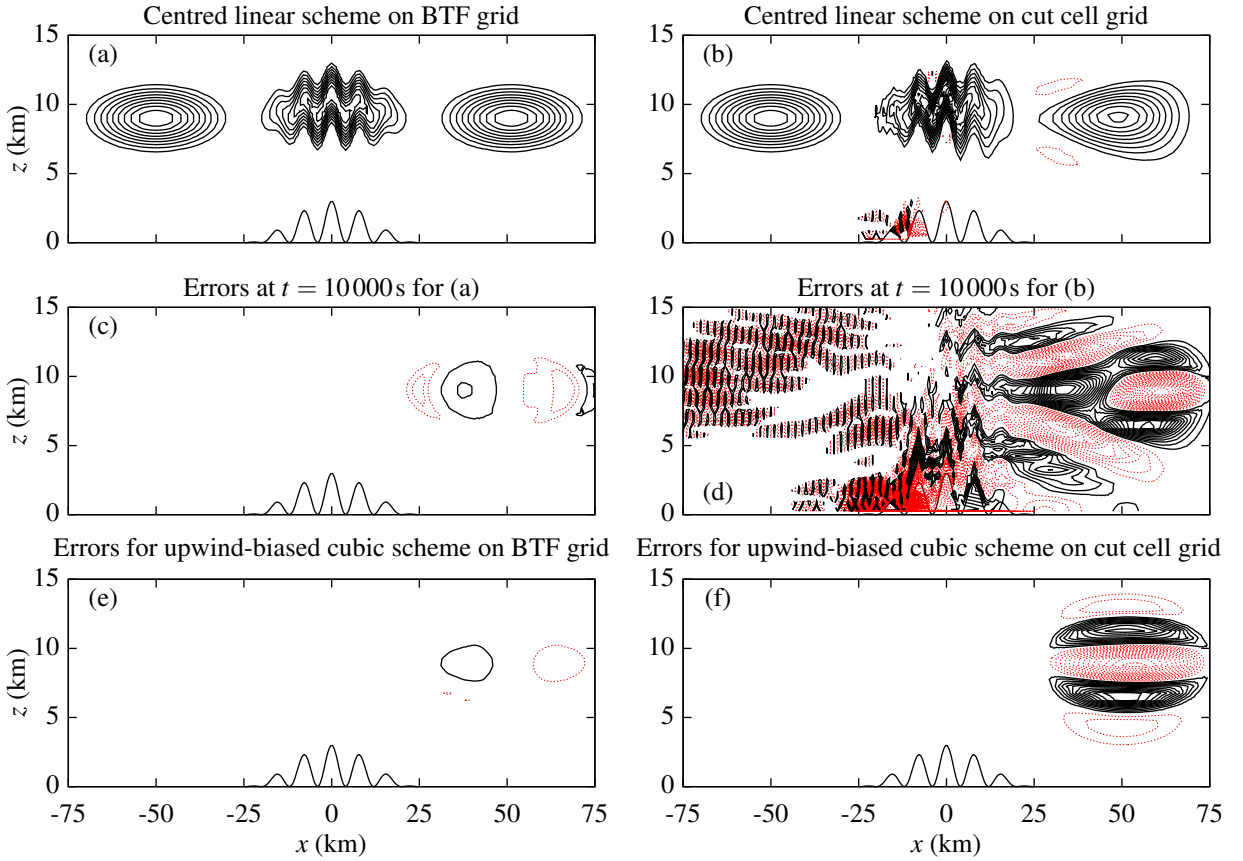




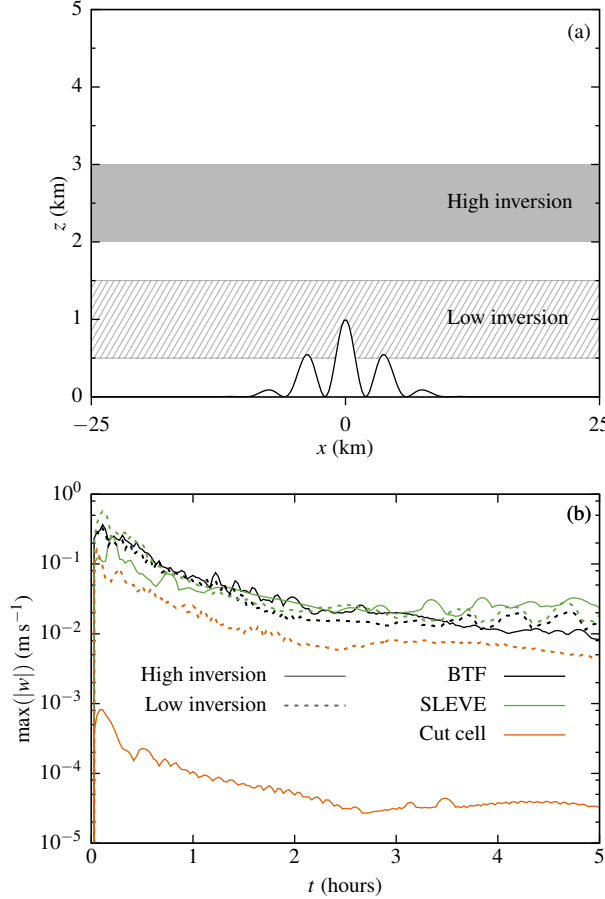
649 FIG. 1. Examples of (a) BTF, (b) SLEVE, and (c) a cut cell grid, showing cell edges in the lowest four layers.  
 650 The full two dimensional grids are 20 km wide and 20 km high. SLEVE parameters are specified in the resting  
 651 atmosphere test in section 4c. The cut cell grid was created by intersecting the terrain surface with a regular grid  
 652 as described in section 2. Axes are in units of m.



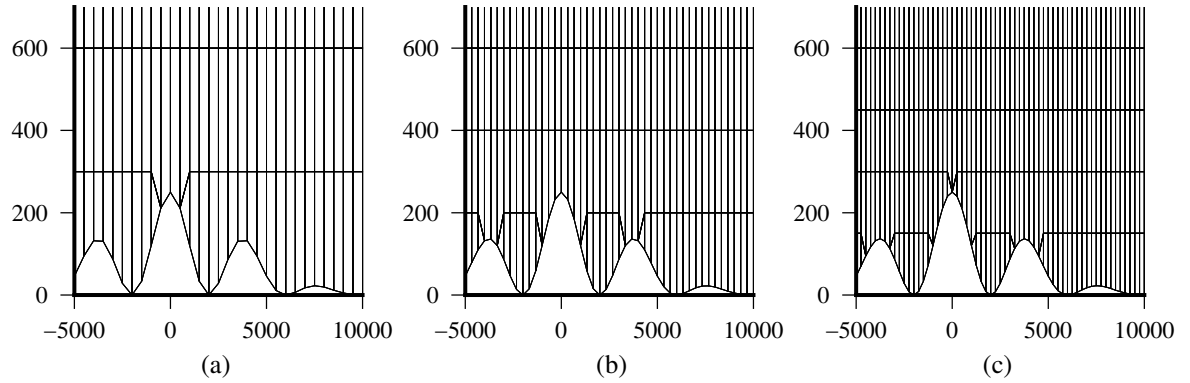
653 FIG. 2. Illustration of a cut cell grid (a) before, and (b) after construction. The terrain surface, denoted by a  
 654 heavy dotted line, intersects a uniform rectangular grid comprising six cells,  $c_1, \dots, c_6$ . The cell vertices, marked  
 655 by open circles, are moved to the points at which the terrain intersects vertical cell edges, marked by filled  
 656 circles. Cells that have no volume are removed. Where a cell has two vertices occupying the same point, the  
 657 zero-length edge that joins those vertices is removed. In this illustration, cells  $c_5$  and  $c_6$  are removed because  
 658 they have no volume, and the zero-length edge at point  $q$  is removed to create a triangular cell,  $c_4$ . Point  $p$  is  
 659 moved down because it is within  $2\Delta z/5$  of the surface, avoiding the creation of a thin cell.



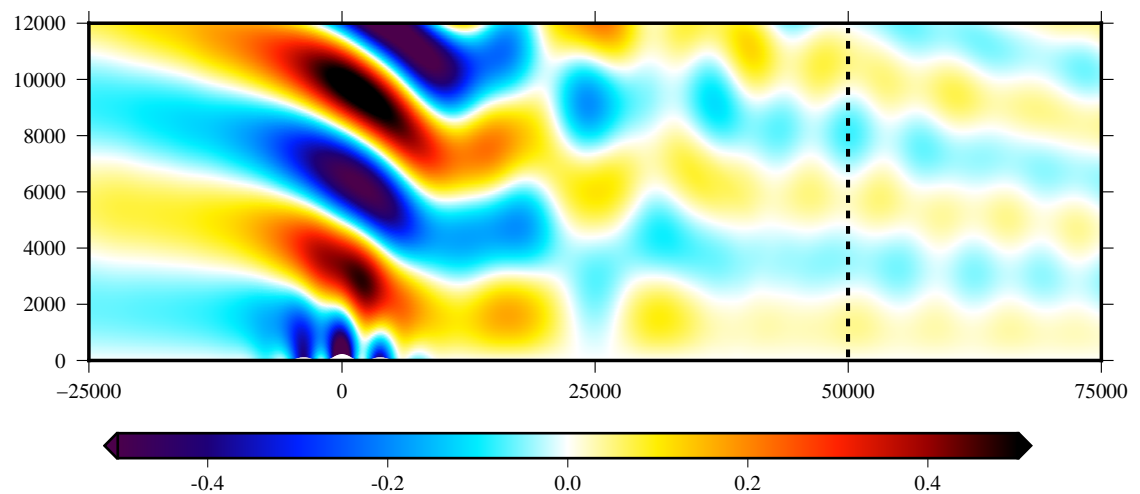
660 FIG. 3. Tracer contours advected in a terrain following velocity field at  $t = 0$  s, 5000 s and 10 000 s using the  
 661 centred linear scheme on (a) the BTF grid, and (b) the cut cell grid with contour intervals every 0.1. Errors at  
 662  $t = 10 000$  s are shown for (c) the centred linear scheme on the BTF grid, (d) the centred linear scheme on  
 663 the cut cell grid, (e) the upwind-biased cubic scheme on the BTF grid, and (f) the upwind-biased cubic scheme  
 664 on the cut cell grid with contour intervals every 0.01. Negative contours denoted by dotted lines. The terrain  
 665 profile is also shown immediately above the  $x$  axis.



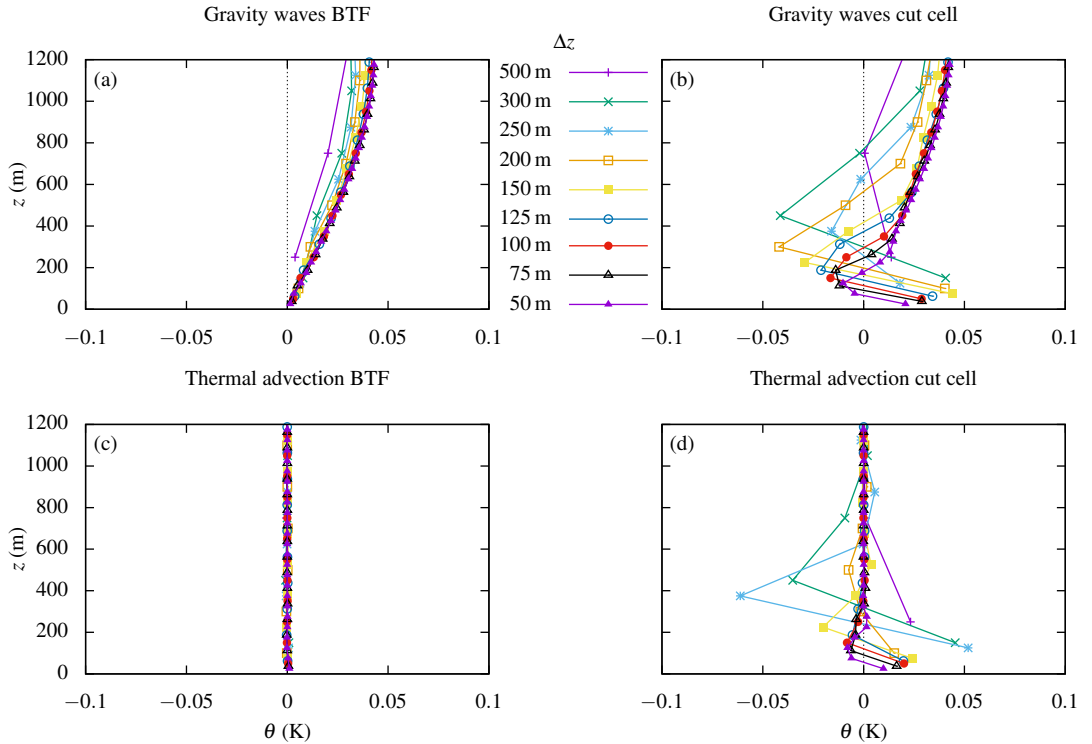
666 FIG. 4. Setup and results of a stratified atmosphere initially at rest. Tests are performed on four grids for two  
 667 different stability profiles, with panel (a) showing the placement of the inversion layer in the two profiles. The  
 668 low inversion is positioned so that it intersects the terrain, shown immediately above the  $x$  axis. In each test,  
 669 the inversion layer has a Brunt-Väisälä frequency  $N = 0.02 \text{ s}^{-1}$ , and  $N = 0.01 \text{ s}^{-1}$  elsewhere. Panel (b) shows  
 670 the maximum magnitude of spurious vertical velocity,  $w$  ( $\text{m s}^{-1}$ ), with results on BTF, SLEVE, cut cell and  
 671 regular grids using the model from Weller and Shahrokhi (2014) which includes a curl-free pressure gradient  
 672 formulation. Results for the high inversion test are shown with solid lines, the low inversion test with dashed  
 673 lines.



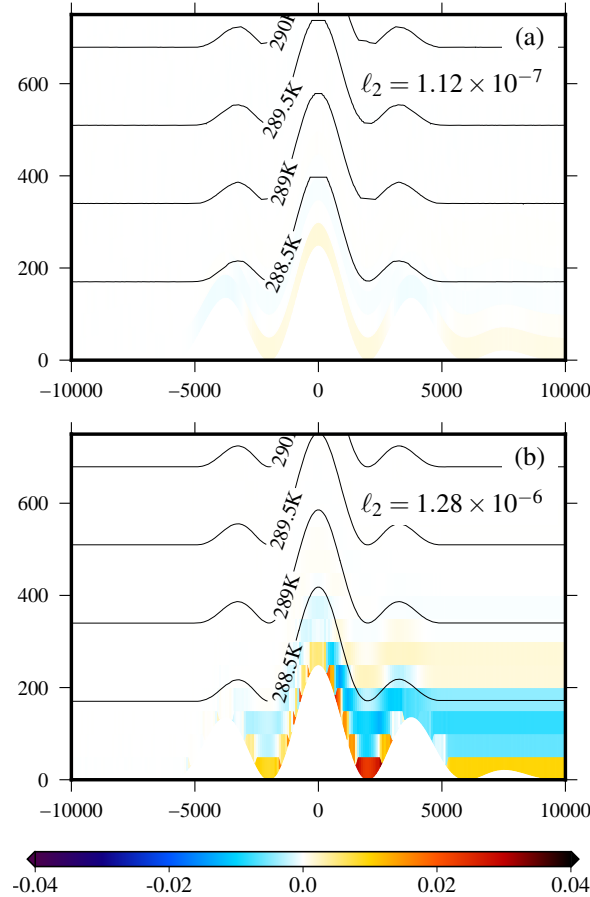
674 FIG. 5. Cut cell grids used for the gravity waves and thermal advection tests at (a)  $\Delta z = 300$  m, (b)  $\Delta z = 200$  m,  
 675 and (c)  $\Delta z = 150$  m. The mountain peak  $h_0 = 250$  m. At  $\Delta z = 300$  m and  $\Delta z = 200$  m, the grid creation process  
 676 has merged small cells with the cells in the layer above but, at  $\Delta z = 150$  m, small cells have been retained. The  
 677 full two dimensional grids are 300 km wide and 30 km high. Axes are in units of m.



678 FIG. 6. Differences in potential temperature between the start and end of the gravity waves test on the BTF  
 679 grid with  $\Delta z = 50$  m. The dashed line at  $x = 50$  km marks the position of the vertical profile in figure 7. Axes are  
 680 in units of m.



681 FIG. 7. Vertical profiles of potential temperature differences between the start and end of the gravity waves  
 682 test on (a) the BTF grid, and (b) the cut cell grid. Results are compared with thermal advection tests results,  
 683 showing differences in potential temperature between the numeric and analytic solutions at  $t = 18000$  s on (c)  
 684 the BTF grid, and (d) the cut cell grid. The results are convergent, except for errors found in the lowest layers  
 685 on the cut cell grids.



686 FIG. 8. Error in potential temperature (measured in K) in the thermal advection test at a resolution of  $\Delta z = 50$  m  
 687 on (a) the BTF grid, and (b) the cut cell grid. Errors are negligible on the BTF grid, but on the cut cell grid errors  
 688 are generated near mountainous terrain and are advected horizontally on the lee side. Contours of the potential  
 689 temperature field at  $t = 18000$  s are overlaid. Axes are in units of m.